ACS APPLIED MATERIALS & INTERFACES

www.acsami.org

Research Article

Amorphization-Driven Lithium Ion Storage Mechanism Change for Anomalous Capacity Enhancement

Sang-eun Bak, Woowon Chung, Muhammad A. Abbas,* and Jin Ho Bang*

Cite This: ACS Appl. Mater. Interfaces 2023, 15, 34874−34882

Read Online

ACCESS | Metrics & More | Article Recommendations | Supporting Information

ABSTRACT: Capacity fading as a function of lithiation/delithiation cycles is a major limitation of Li-ion batteries. Most Li storage materials are susceptible to this phenomenon due to the degradation of the crystal structure and particle integrity as a result of volume changes associated with lithiation/delithiation processes and/or irreversible redox reactions. However, some Li storage materials show an increase in capacity with an increase in cycles; this phenomenon has been termed "negative fading." Negative fading in Li host materials is usually associated with the additional charge storage at the particle/solid−electrolyte interface (SEI) layer, decomposition/formation of the SEI layer, or redox reactions of various Li species at the interface. In this work, we report the observation of negative fading in a newly discovered anode material, $TiNbO_4$ (TNO), and reveal amorphization as a new mechanism for negative fading in Li host materials. This assertion was confirmed via a close relationship between changes in the crystal structure and the Li storage mechanism in TNO. Given that other titanium niobium oxide analogues (e.g., $TiNb_2O_7$) suffer from capacity loss due to amorphization, this unique electrochemical behavior of TNO may provide an interesting new direction to tune the titanium niobium oxides for high-performance, stable battery anodes.

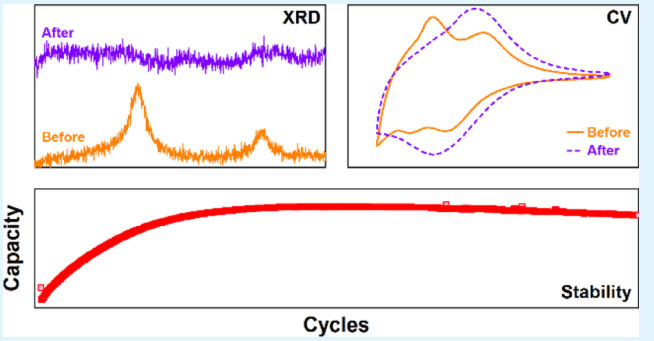

KEYWORDS: *lithium-ion batteries, titanium niobium oxide, amorphization, negative fading, charge storage mechanism*

1. INTRODUCTION

Electrochemical energy storage devices have become a fundamental part of our daily lives, powering almost every portable device used today.[1−3] Even human mobility is becoming rapidly dependent on this technology.[4] Li-ion batteries (LIBs) are the most common such technology. However, the economic and ecological sustainability of the widespread use of LIBs significantly depends on their cycling stability. Significant strides have been made in this regard. The most common approach to addressing this problem is the development of new electrode materials or the surface engineering of particles to protect them from detrimental reactions.[5] However, the lithiation/delithiation reactions occurring during battery operation are accompanied by volume changes and/or irreversible redox reactions.[6−11] As a consequence, structural deterioration of the electrode material is an inevitable process, consequently leading to capacity degradation. Hence, any novel approach that can resolve this fundamental limitation of LIBs can play a breakthrough role in the future of this technology.

An interesting solution to capacity degradation is the use of electrode materials that show anomalous capacity enhancement, which is referred to as negative fading.[12] The capacity of such materials increases with an increase in the number of cycles. Therefore, they can maintain or even show improved capacity for thousands of cycles. However, the reasons for the negative fading observed in LIBs are still a topic of debate.[13] Various mechanisms that can explain this abnormal capacity increase have been suggested, most of which are intimately involved with interfacial events. A mechanism associated with the solid−electrolyte interface (SEI) layer is one of these examples. The SEI layer is an important component of a battery electrode. The SEI layer usually forms during the first few cycles due to electrolyte decomposition on the surface,[14,15] but a stable, solid SEI layer can protect a battery's electrodes from further deterioration.[16,17] Interestingly, the formation and decomposition of secondary SEI layers can help enhance the capacity by providing additional Li-ion storage within the layers.[18,19] Additionally, Rezvani et al. suggested that the formation and decomposition of a surface layer that stems from the electrolyte might cause negative fading in carbon-

Received: April 13, 2023
Accepted: June 28, 2023
Published: July 12, 2023

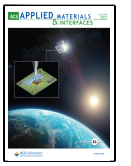

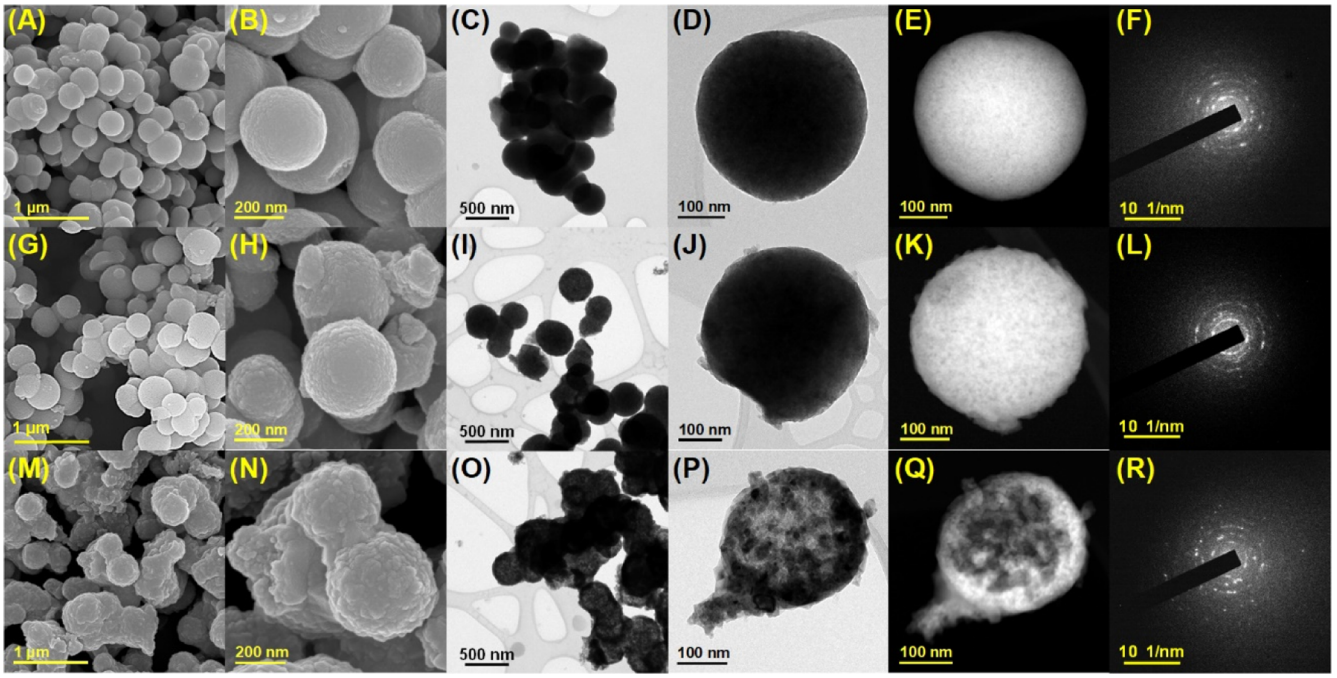

Figure 1. (A,B,G,H,M,N) SEM images, (C,D,I,J,O,P) TEM images, (E,K,Q) dark-field TEM images, and (F,L,R) SAED patterns of (A−F) TNO-600, (G−L) TNO-700, and (M−R) TNO-800 samples.

coated $ZnFe_2O_4$.[20] Another reported mechanism is interfacial charge storage. Li ions can form various compounds, such as LiF and Li_2O, on the solid layer of the particle surface; these can act as an additional Li-ion reservoir.[21,22] This mechanism was observed to be responsible for negative fading in TiO_2 and Ru_2O anodes.[23,24] Surface redox reactions of Li to reversibly form various species represent another type of reported mechanism.[25,26]

Despite the progress in understanding the stability of LIBs, there is still much uncertainty regarding the origin of negative fading. However, one thing is certain; the mechanism of negative fading significantly depends on the anode material type and battery architecture. Here, we report another possible mechanism of negative fading appearing in a recently discovered anode material: $TiNbO_4$ (TNO). Unlike other titanium niobium oxide analogues (e.g., $TiNb_2O_7$, $Ti_2Nb_{10}O_{29}$, $TiNb_6O_{17}$, and $TiNb_{24}O_{62}$),[27] the rutile-phased TNO is an intrinsic intercalation pseudocapacitive Li storage material, i.e., the Li storage in TNO is pseudocapacitive in nature and accompanied by bulk Faradaic processes.[28,29] Moreover, the rate performance of TNO is independent of the surface area and nanostructure of the particles.[28] Interestingly, while exploring the nanostructuring effect of TNO in this work, we observed that, unlike other nanostructured titanium niobium oxide families that show gradual capacity degradation over cycling, nanostructured TNO is highly stable and can even see a boost in its initial capacity over long-term cycling. However, this newly observed negative fading in TNO cannot be explained by any of the mechanisms proposed so far. Hence, we performed an in-depth study to trace the Li storage mechanism occurring in TNO as a function of cycles, from which we concluded that the likely reason for the increase in the capacity of TNO is the change of the Li storage mechanism from intercalation pseudocapacitance to surface pseudocapacitance, which is driven by amorphization.

2. EXPERIMENTAL SECTION

2.1. Chemicals and Materials. Ti and Nb precursors, i.e., titanium(IV) butoxide (97%) and niobium(V) ethoxide (99.999%, metal basis), were obtained from Merck and Alfa Aesar, respectively. Lithium metal foil (99.9%) was also purchased from Alfa Aesar. Polyvinylidene fluoride (PVDF) powder with an average molecular weight of 534,000 (as determined by GPC) and ethylene glycol were purchased from Merck. The $LiPF_6$-based electrolyte, Celgard-2400 membrane, and Super P were bought from Wellcos Co. Ltd. Acetone, ethanol (99.9%), *N*-methyl-2-pyrrolidone (NMP, ≥99.5%), and acetic acid (≥99.5%) were acquired from Daejun Chemical and Metals Co. Ltd.

2.2. Synthesis. TNO powder was synthesized by a method reported previously.[28,29] Briefly, to synthesize the TNO precursor, ethylene glycol (40 mL) was taken in a 300 mL beaker and placed under stirring (500 rpm). Then, titanium butoxide (0.05 mL) and niobium ethoxide (0.04 mL) were added to ethylene glycol using a syringe. Reactants were sealed with Parafilm and stirred for 30 min. Then, a solution containing acetone and deionized water (99:1, 100 mL) was added, and the reactants were stirred for another 1 h. The obtained product was washed three times with ethanol via centrifugation and dried at 60 °C. All the processes for the synthesis of the TNO precursor were carried out in a glove box with an N_2 atmosphere and 15% humidity. The TNO precursor was calcined at various temperatures (600, 700, and 800 °C) for 2 h; before the heating process, the furnace was purged with N_2 for 2 h to remove trace O_2. The heating rate was 10 °C min^{-1}.

2.3. Material Characterization. X-ray diffraction (XRD) patterns were acquired with a Bruker diffractometer (D2 Phaser), and TOPAS v5 software was used for Rietveld analysis. Scanning electron microscopy (SEM) and transmission electron microscopy (TEM) were carried out using Hitachi S-4800 and JEOL JEM-2100F electron microscopes. Thermogravimetric analysis (TGA) and differential scanning calorimetry (DSC) analyses were implemented using a thermal analyzer (SDT-Q600, TA Instruments) under airflow. The particle surface area and pore size distribution were analyzed by acquiring N_2 adsorption/desorption isotherms at 77 K using a BELSORP-mini-II made by BEL Japan. The specific surface area and pore-size distributions were determined using the Brunauer−Emmett−Teller (BET) and Barrett−Joyner−Halenda (BJH) meth-

https://doi.org/10.1021/acsami.3c05324
ACS Appl. Mater. Interfaces 2023, 15, 34874−34882

ods, respectively. Electron paramagnetic resonance (EPR) spectra were taken at 120 K using a Bruker EMXplus EPR spectrometer, and the carbon contents of TNO samples were determined using a FLASH EA 1112 organic elemental analyzer manufactured by Thermo Fisher Scientific, Co.

2.4. Cell Fabrication and Electrochemical Characterization. The active material (TNO samples) was mixed with Super P and PVDF in a 6:2:2 ratio in NMP as a solvent and turned into a uniform slurry using a mortar grinder. Cu foil was used as a current collector, and a film applicator was used to apply the active material slurry and prepare a uniform thin film. This film was then placed in a vacuum oven at 120 °C for 12 h for drying. Afterward, it was passed through a rolling presser to attain a 20 μm thick film, and 11 mm diameter electrodes were punched out of the film. The loading mass of the active material in all the experiments was ~1.0 mg cm^{-2}. LIB half-cells were assembled with the TNO working electrode (11 mm in diameter punched from the film prepared on the Cu foil), a $LiPF_6$-based commercial electrolyte (1 M $LiPF_6$ in ethylene carbonate/dimethyl carbonate = 1:1), Celgard 2400 membrane as the separator, and Li-metal foil as the counter electrode. The whole assembly process was performed in an argon-filled glove box. Lithiation/delithiation cycling of the half-cells was performed using WonATech WBCS3000 battery cyclers, and a ZIVE BP2 potentiostat was used for electrochemical impedance spectroscopy (EIS) analysis.

3. RESULTS AND DISCUSSION

The TNO precursor consisted of smooth spherical particles with a particle size of ~500 nm (Figure S1), and it was a purely amorphous phase (Figure S2). To obtain nanostructured TNO, the precursor was heated under an N_2 atmosphere because a completely oxygen-free atmosphere was compulsory to obtain a pure TNO phase, as noted previously.[29] According to TGA and DTA analyses, the precursor begins to decompose at 300 °C (Figure S3), but a temperature of 550 °C was required to observe the formation of the crystalline phase (Figure S2). Further temperature increases improved only the material's crystallinity without transforming it into other phases. TNO samples prepared at 600, 700, and 800 °C were explored in this work, and they will hereafter be referred to as TNO-600, TNO-700, and TNO-800, respectively.

Similar to the precursor, all TNO samples consisted of smooth spherical particles (Figure 1). However, increasing the calcination temperature to 800 °C did cause some surface morphological changes. Although the overall particle shape was preserved in TNO-800, particles became aggregated to some extent and the surface became rougher (Figure 1M,N). The dark-field TEM images (Figure 1E,K,Q) revealed the presence of internal porosity in all TNO samples. The pore size in TNO-600 seemed to be very small but grew in size in TNO-700. However, at a calcination temperature of 800 °C, the small pores merged to form large voids in TNO-800 (Figure 1P,Q). The N_2 physisorption isotherm analysis affirmed the presence of pores (Figure S4). The analysis results revealed that the BET surface areas of TNO-700 and TNO-800 were 90.7 and 111.3 m^2 g^{-1}, respectively (Table S1). Interestingly, however, the surface area of TNO-600 was only 6.5 m^2 g^{-1}, implying that TNO-600 contained mostly closed pores. Nevertheless, TEM micrographs clearly pointed toward the existence of internal porosity in TNO-600. On the other hand, the selected area electron diffraction (SAED) analysis of all samples indicated an increase in crystallinity with increasing calcination temperature (Figure 1F,L,R).

The XRD analysis (Figure 2) revealed that all the TNO samples consisted of the pure $TiNbO_4$ phase, regardless of the calcination temperature (see Table S2 for Rietveld refinement

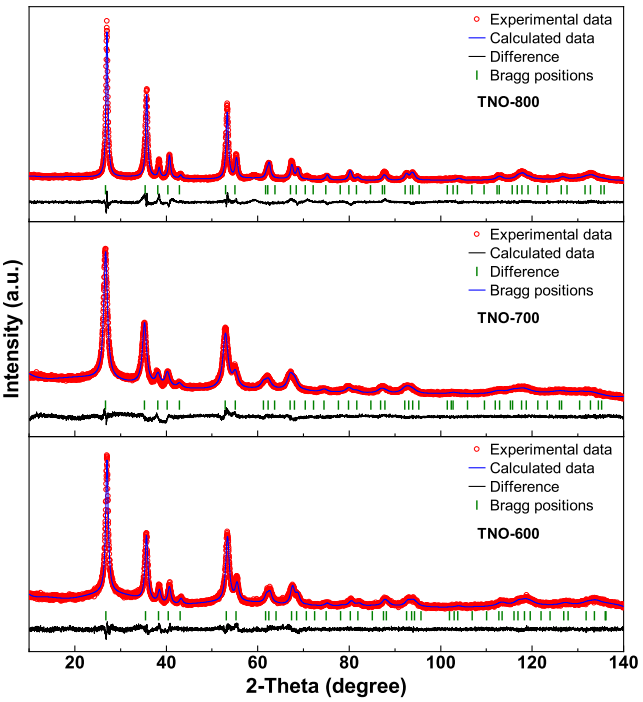

Figure 2. XRD and Rietveld refinement of TNO-600, TNO-700, and TNO-800 samples.

results). However, increasing the calcination temperature had some influence on the crystallinity and lattice defects. Grain sizes (determined using the Scherrer equation) increased from 11.0 to 21.3 nm as the calcination temperature was increased from 600 to 800 °C (Table S2), which is consistent with the observations made in the SAED analysis. As the calcination process was carried out in a reducing environment and many organic species were present in the TNO precursor, carbon contents were analyzed to determine the residual carbon present in the samples. Elemental analysis revealed the presence of small amounts of carbon in all of the samples, but the amount of carbon decreased from 9.62 to 6.96% when the calcination temperature increased from 600 to 800 °C (Table S2). As revealed in our previous study,[29] the reducing environment created during the synthesis of TNO (i.e., carbothermal reduction) can create oxygen vacancies. Indeed, EPR spectra affirmed the presence of oxygen vacancies in TNOs, which was evidenced by a signal appearing at a g-value of 2.001 (Figure S5). Also, the amount of oxygen vacancies correlates with the carbon content of the TNO samples.

The as-prepared TNO materials were used as the active anode material in the battery half-cell configuration, with Li metal as the counter electrode. The discharge capacity of TNO-600 was 140 mA h g^{-1} at 1C, which decreased to 82 mA h g^{-1} in TNO-800 (Figure 3A). The higher capacity in TNO-600 could be attributed to the presence of oxygen vacancies and its higher carbon content.[29] $TiNbO_4$ stores most of the Li ions in the (110) and (200) planes via intercalation pseudocapacitance, which can be detected as a gradual change in the galvanostatic charge/discharge curves.[29] Indeed, all the samples in the current work showed a gradual incline/decline in their voltage profiles, and no voltage plateau region was observed (Figure 3B–D). This result indicates the absence of a phase transformation mechanism and the presence of a pseudocapacitive Li storage mechanism, irrespective of the

https://doi.org/10.1021/acsami.3c05324
ACS Appl. Mater. Interfaces 2023, 15, 34874−34882

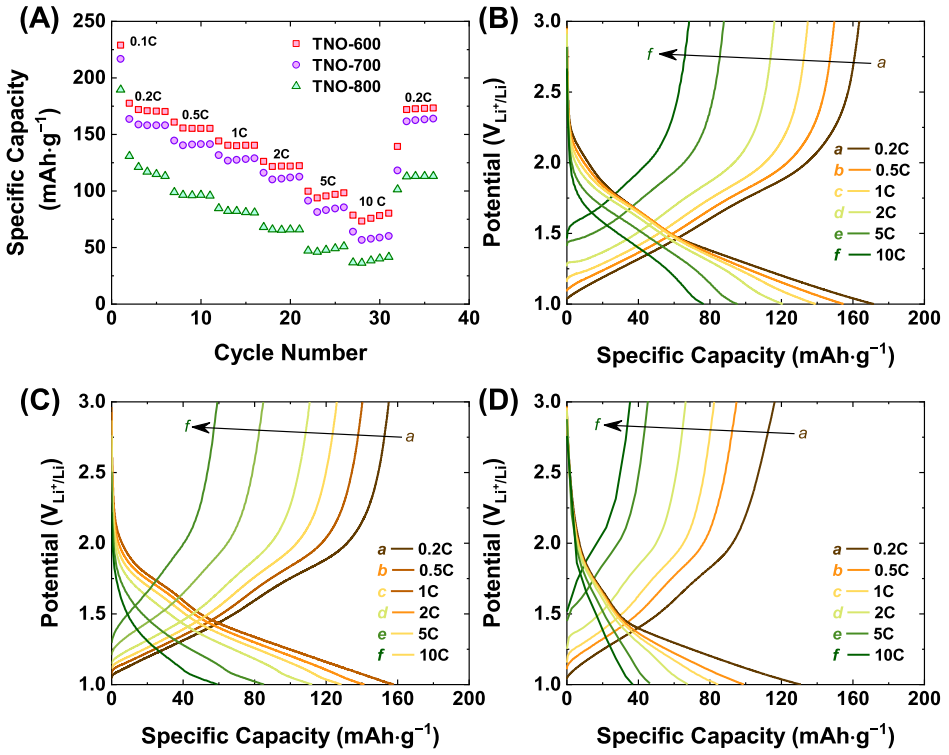

Figure 3. (A) Rate performance and corresponding voltage profiles of (B) TNO-600, (C) TNO-700, and (D) TNO-800.

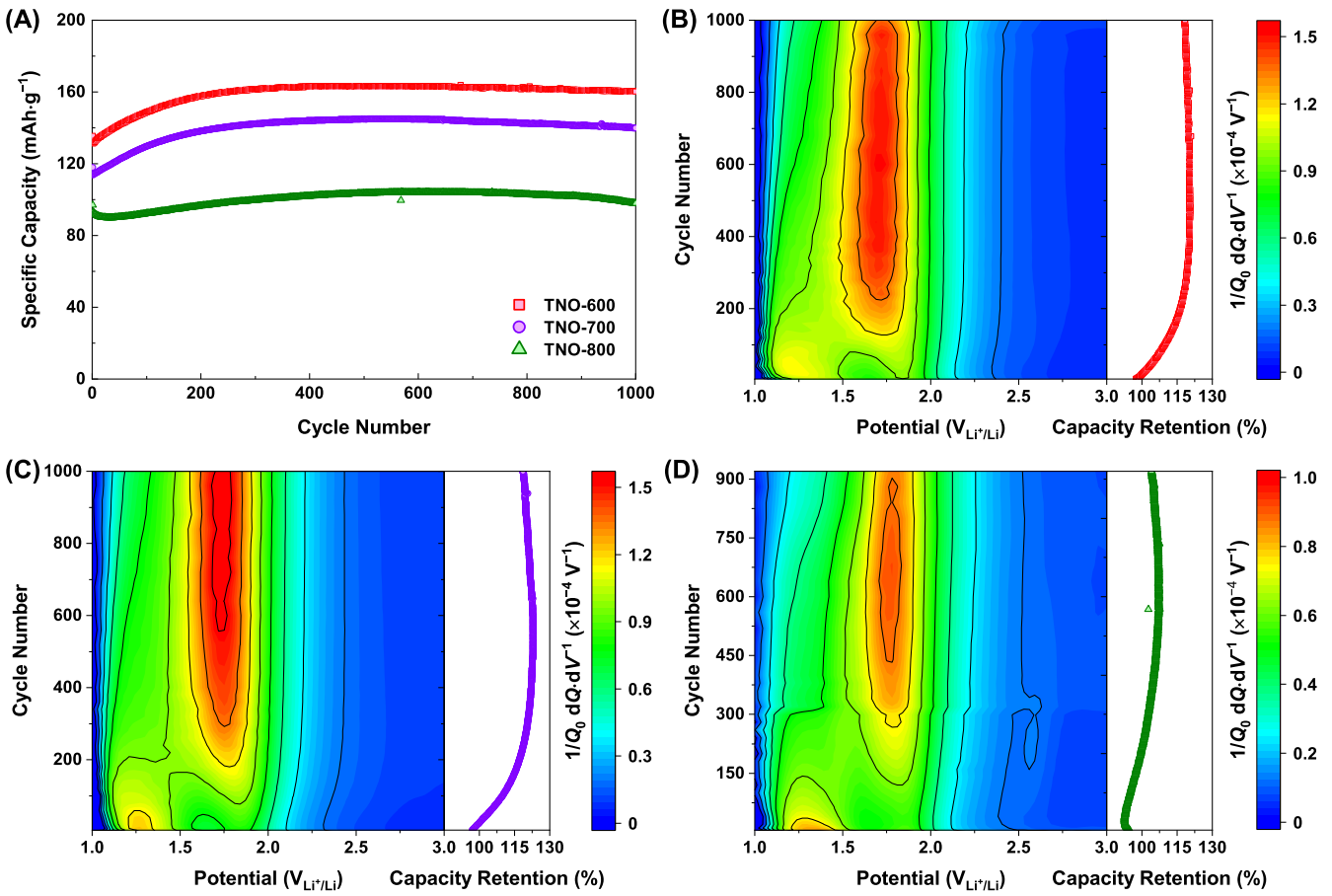

Figure 4. (A) Specific capacities of TNO-600, TNO-700, and TNO-800 as a function of the number of cycles at 1C. The differential capacity (dQ dV^{-1}) contour maps of delithiation profiles and percentage capacity retention of (B) TNO-600, (C) TNO-700, and (D) TNO-800 during the long-term stability test.

https://doi.org/10.1021/acsami.3c05324
ACS Appl. Mater. Interfaces 2023, 15, 34874−34882

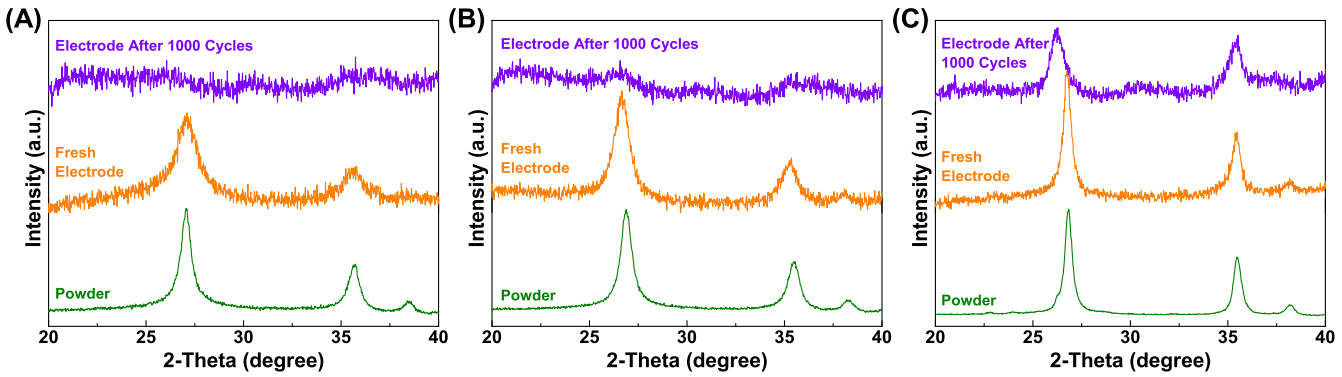

Figure 5. XRD patterns of (A) TNO-600, (B) TNO-700, and (C) TNO-800 as powder, fresh electrodes, and electrodes after 1000 cycles.

surface area and grain structure; this is consistent with previous reports investigating the Li storage mechanism in TNO.[28−31]

Long-term stability is a crucial requirement for battery electrode materials for practical applications. In general, the discharge capacity of LIB electrode materials fades away with continuous charging and discharging cycles. However, some battery electrodes show an increase in capacity with an increase in the number of cycles. As discussed earlier, this phenomenon has been termed negative fading.[13] All of our TNO samples were evaluated for long-term stability at 1C for 1000 cycles, and they showed excellent stability (Figures 4A and S6). The capacities of TNO-600, TNO-700, and TNO-800 after 1000 cycles were 118, 119, and 101%, respectively, of the initial capacity. The phenomenon of negative fading was clearly present in all of these samples; for example, the capacity of TNO-600 increased to 120% of the initial capacity after 350 cycles. Another interesting aspect observed in the long-term performance of these nanostructured TNO electrodes was that the rate at which their capacity increased and the number of cycles required to reach the maximum capacity differed significantly. However, the number of cycles required to reach the maximum capacity did show a correlation with the calcination temperature and the initial structure of the material (Figures 4A and S7). For example, 360 cycles were required for TNO-600 to reach its capacity maximum, whereas TNO-800 needed 600 cycles to reach its maximum. In addition, we tested the TNO samples processed at 450 and 550 °C with largely amorphous structures. Indeed, a correlation was observed between the cycles needed to reach the maximum capacity and the processing temperature (i.e., the crystallinity of the samples). However, electrochemical amorphization (i.e., achieved via continuous lithiation/delithiation reactions) seemed more beneficial than amorphization via physical processing (Figure S8), partly because TNO-600 was more stable than TNO-450 or TNO-550. However, more research is needed to clarify this observation.

To obtain more insight into this observation, differential capacity ($dQ\ dV^{-1}$) plots were analyzed to investigate any changes in the Li storage behavior as a function of the number of cycles (Figures 4B−D, S9, and 10). Initially, the $dQ\ dV^{-1}$ curves of TNO showed two distinct anodic peaks at 1.87 and 1.34 V vs Li^+/Li ($V_{Li+/Li}$), which were also evident in the cyclic voltammograms (Figure S11). However, continuous cycling caused the 1.87 V peak to gradually shift to 1.72 V, broaden, and increase in intensity, while the peak at 1.34 V nearly disappeared. Finally, after 1000 cycles, the $dQ\ dV^{-1}$ curves of all TNO samples showed a single broad anodic peak at 1.72 $V_{Li+/Li}$. More interestingly, the number of cycles in each sample, where the shift and growth of the anodic $dQ\ dV^{-1}$ peak appearing at 1.72 V were stabilized, matched perfectly with the number of cycles where the maximum capacity was achieved. This implies that the features of the $dQ\ dV^{-1}$ curves and negative fading in TNO are intimately linked. Since the $dQ\ dV^{-1}$ analysis can be used to ascertain information about the Li storage mechanism of a material, the increase in capacity with cycling is not a result of mere surface or structural stabilization. Instead, the fundamental Li storage behavior of TNO may have been changed. Given the $dQ\ dV^{-1}$ results and galvanostatic charge/discharge profiles, we concluded that cycling resulted in the change of the Li storage mechanism from intercalation pseudocapacitance to surface pseudocapacitance.

To shed light on the structural changes that occurred during the long-term operation, XRD analysis was performed on the battery electrodes before and after cycling to understand any changes in the material crystal structure due to cycling. As presented in Figure 5, the XRD patterns of fresh electrodes match very well with the diffraction peaks of the powder TNO sample, but considerable changes were observed in the XRD patterns of the electrodes obtained after cycling. In TNO-600 and TNO-700, XRD peaks almost completely disappeared (crystallinity was lost even after 500 cycles as seen in Figure S12), indicating the absence of any significant level of crystallinity in the samples after cycling. However, low-intensity, very broad peaks can still be observed, indicating the presence of the TNO phase, albeit in near-amorphous conditions. Unlike TNO-600 and TNO-700, relatively clear and high-intensity XRD peaks were observed in TNO-800 after cycling. A closer look at the XRD pattern revealed that the peak at 27° shifted to a lower 2-theta value, although the peak at 35.5° did not show any shift. In the TNO phase, most of the Li intercalation occurs in the (110) plane centered at 27°, whereas the participation of the (101) plane appearing at 35.5° is not significant in Li intercalation.[29] Hence, Li intercalation through the (110) plane led to the deterioration of the (110) plane, which resulted in the expansion of the plane and subsequent peak shift. These results suggested that the crystal structure of TNO was damaged during cycling via the amorphization of the particles. However, the extent of amorphization was not consistent in all samples. TNO-600 particles contained a large amount of internal porosity and had the smallest grain size, which could be the reason for the more rapid amorphization of TNO-600 compared to the other samples. In TNO-800, however, a higher level of crystallinity was preserved after cycling, indicating the dependence of

https://doi.org/10.1021/acsami.3c05324
ACS Appl. Mater. Interfaces 2023, 15, 34874−34882

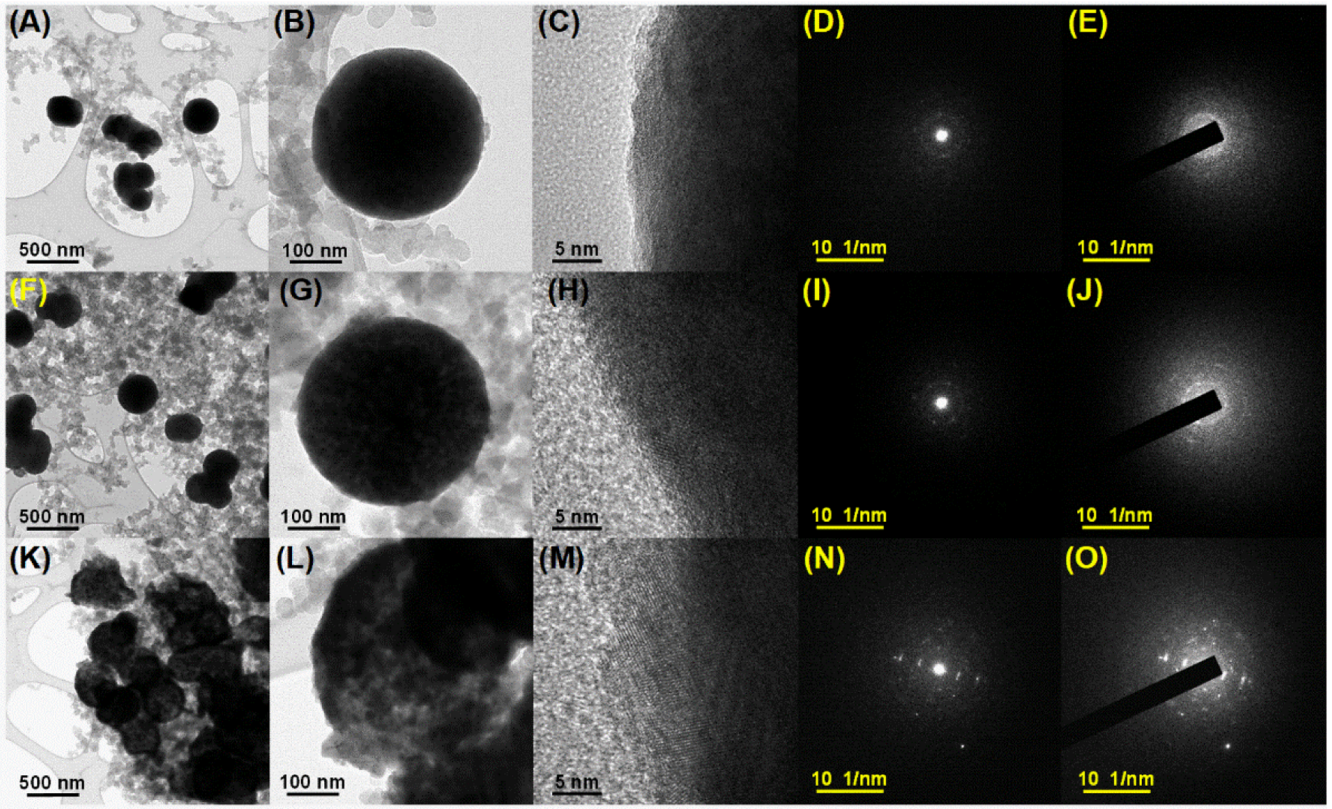

Figure 6. (A,B,F,G,K,L) TEM images, (C,H,M) high-resolution TEM images, and (D,E,I,J,N,O) SAED patterns of (A−E) TNO-600, (F−J) TNO-700, and (K−O) TNO-800 samples after 1000 cycles at 1C.

cycling-induced amorphization on the material's initial crystallinity and porous structure.

As observed by the microscopic analysis (Figure 1), TNO particles had a solid spherical morphology and a porous structure with well-defined crystallinity. Even after cycling, the morphology of the particles was well preserved (Figure 6). However, noticeable changes were observed in the crystallinity, as observed in our XRD analysis. The lattice fringes were barely observable in TNO-600 and TNO-700 (Figure 6C,H), but those in TNO-800 were more visible in the TEM image (Figure 6M). The SAED analysis results were in good accordance with this observation. The SAED patterns of TNO-600 (Figure 6D,E) and TNO-700 (Figure 6I,J) showed no distinguishable ring patterns, indicating the presence of a completely amorphous phase. However, TNO-800 SAED patterns were consistent with a polycrystalline phase (Figure 6N,O). Therefore, the TEM analysis reaffirmed the conclusions made by our XRD analysis; cycling resulted in the amorphization of the TNO structure.

EIS analysis was employed to further investigate the interfacial charge transfer processes. The Nyquist spectra of the TNO samples (Figure 7A−C) showed three semicircles and a low-frequency capacitive tail, which is a common observation in Li-ion storage materials.[32−36] The first semicircle in the high-frequency region is attributed to the charge-transfer resistance through the SEI layer (R_{SEI}). The second semicircle originates from the interfacial charge-transfer resistance at the electrolyte/particle interface (R_{ct}). The last circle results from the diffusion of Li ions within the TNO particles (R_{Li}). The equivalent circuit used for fitting is given in Figure S13, and the fitting results are presented in Figure 7D−I. The R_{SEI} values of all TNO samples significantly increased after cycling (Figure 7D−F), while their capacity was higher at the end of the stability test than at the start. At a glance, this may look strange; however, the fitting results are consistent with the experimental data, where a clear growth of the first circle is observed after cycling (Figure 7A−C). Hence, this result can be rationalized by keeping in view that cycling can result in the formation of a thicker/poor-quality SEI layer that leads to a higher R_{SEI} value. It is noteworthy that one may argue that the formation of electrolyte-derived surface layers (e.g., SEI) can be one of the reasons for the observed capacity boosting of TNO over cycling. If Li ions were being stored in the SEI layer, it would cause significant changes in the SEI layer, which can also lead to a substantial change in the R_{SEI} during a lithiation/delithiation cycle. Many LIB anodes showed the formation of an SEI layer below 1 V potential that may be able to store additional Li ions. Hence, as a control experiment, we cycled TNO-600 between 0 and 3 V potential window. Indeed, an SEI layer formation plateau was observed near 0.8 V (Figure S14A), and as a result, the Li storage capacity of TNO-600 in the 0−3 V potential window was significantly greater than the theoretical capacity. Moreover, R_{SEI} showed a significant jump during the lithiation process (Figure S14B,C), indicating the storage of Li ions in the SEI layer. However, in all our samples, which were cycled between 1 and 3 V, no abrupt or gradual change in R_{SEI} was observed, indicating that the SEI layer does not play a significant role in Li storage in the 1−3 V potential window. Moreover, in previous reports, which are associated with negative fading due to additional Li storage in the SEI layer, this mechanism appeared only after the surface layers were optimized; initial capacity fading was followed by a gradual increase in capacity.[13,37] In our case, however, as there was almost no

https://doi.org/10.1021/acsami.3c05324
ACS Appl. Mater. Interfaces 2023, 15, 34874−34882

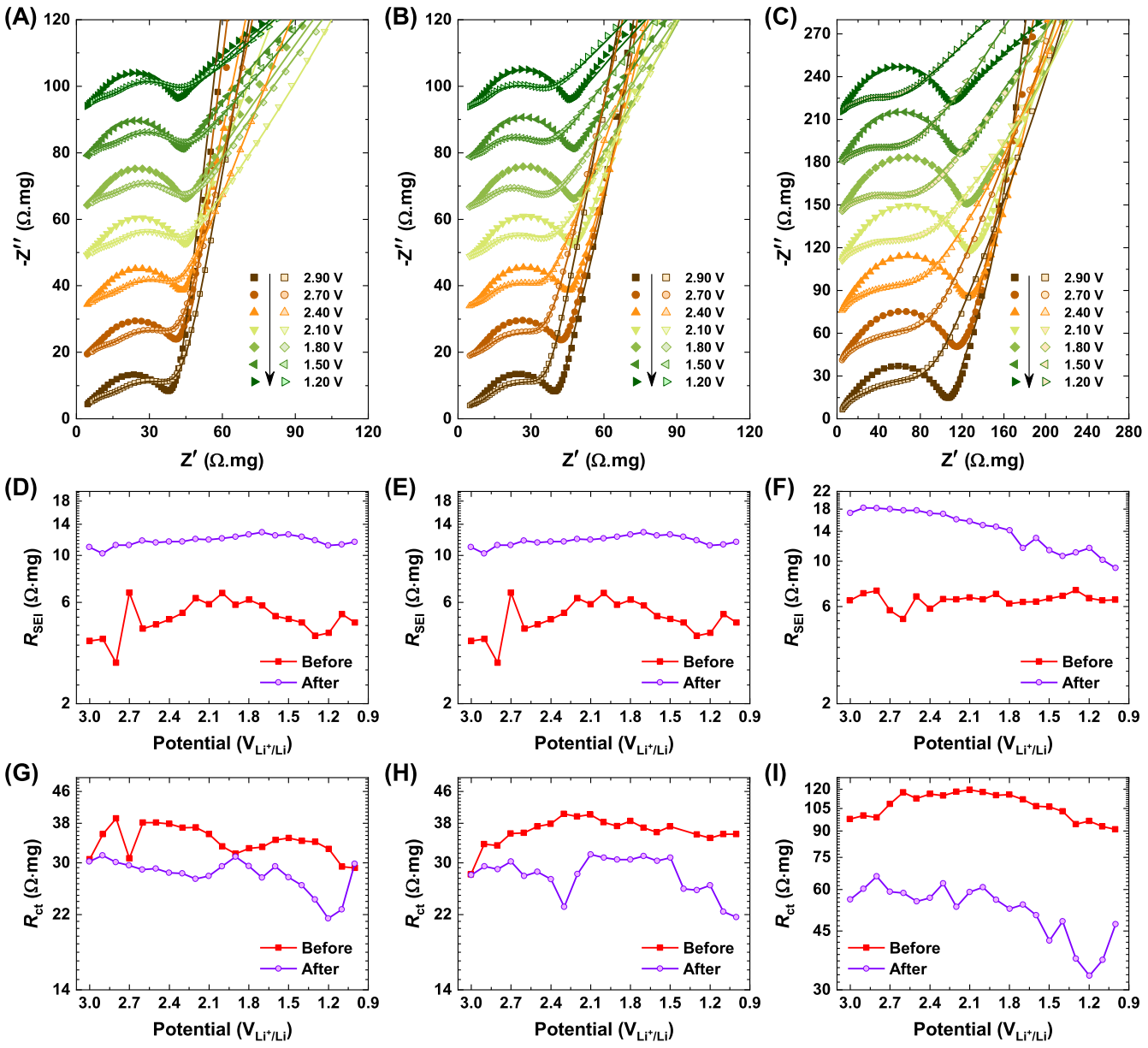

Figure 7. (A–C) Nyquist plots, (D–F) R_{SEI}, and (G–I) R_{ct} of (A,D,G) TNO-600, (B,E,H) TNO-700, and (C,F,I) TNO-800 during lithiation before and after 1000 cycles at 1C. In panels A–C, the solid and open symbols represent samples before and after 1000 cycles, respectively, and the symbols and solid lines represent experimental data and fitted lines, respectively.

initial capacity fading, we presumed that the possible contribution from the electrolyte-derived surface layer could be excluded. Any possible contribution from this mechanism would be insignificant. TNO-800 did show a slight initial capacity decrease, but that decrease was significantly small compared with the previous reports.[12] On the other hand, the R_{ct} values of all samples decreased after cycling (Figure 7G–I), indicating that the increase in capacity must have stemmed from improvements in the interfacial charge transfer kinetics. The underlying reason for the facilitated charge transfer kinetics remains elusive, but it is apparent that amorphization and the resulting change in the Li storage mechanism play a critical role in this enhancement.

As discussed earlier, negative fading in Li storage materials can appear due to various mechanisms. Some Li host materials (e.g., Fe_2O_3, Cu_2O, and CoO) can store additional charge with an increase in cycles due to the continuous formation and decomposition of the SEI layer, which results in a capacity that is even higher than their theoretical capacity.[20,38] This mechanism has been observed in Li host materials that store charge via the conversion reaction mechanism. Additional Li storage capacity can also be attained by storing Li ions at metal/Li_2O interfaces, such as Ti/Li_2O, Ru/Li_2O, and Co/Li_2O, which can lead to negative fading.[23,24,39] The redox reactions of species containing Li that accumulate on the surface of the particles during cycling represent another reported mechanism of negative fading in Li storage materials.[26,40,41] While this anomalous capacity boosting has yet to be fully elucidated, Yoon and co-workers recently shed light on this exotic phenomenon by classifying various causes of negative fading into three cases: (i) facilitated conversion reactions, (ii) additional utilization of surface layers, and (iii) morphological changes.[13] However, based on our in-depth electrochemical analysis and post-mortem characterization,

https://doi.org/10.1021/acsami.3c05324
ACS Appl. Mater. Interfaces 2023, 15, 34874–34882

none of these mechanisms can account for the capacity enhancement observed in our TNO electrodes. Therefore, based on our investigation, we concluded that an amorphization-driven lithiation capacity increase in TNO would be a rational cause for the observed negative fading. This amorphization has a significant influence on the Li storage mechanism, which can facilitate the interfacial charge transfer kinetics and increase the specific capacity.

It should be noted that amorphization does exist in analogue oxides or titanium and niobium; for example, $TiNb_2O_7$ shows structural amorphization upon cycling. However, amorphization in $TiNb_2O_7$ leads to capacity degradation.[42] Therefore, the charge storage capacity increase upon amorphization seems to be a unique aspect of TNO. The reason for this disparity remains elusive, but we hypothesized that the existence of the +4 only oxidation state of Nb in TNO may be linked to the anomalous capacity enhancement. Unlike other oxides of titanium and niobium that contain Nb in mixed oxidation states (+4 and +5), charge neutrality demands the presence of only the +4 state for the rutile phase TNO.[29] However, the structural degradation of TNO may enable Nb to change its oxidation state up to +5, which can lead to additional charge storage. We caution that this is just speculation at present; hence, further research is underway to elucidate the uniqueness of amorphization in TNO.

4. CONCLUSIONS

Nanostructured TNO exhibits the phenomenon of negative fading. Unlike conventional mechanisms for negative fading, however, there are two different aspects of negative fading in TNO. First, the number of cycles required to reach the maximum capacity depends on the initial structure of the particles. Second, negative fading in all samples is driven by amorphization. Our investigation revealed that, under continuous cycling, the Li storage mechanism gradually shifted from intercalation pseudocapacitance to surface pseudocapacitance. This shift gave rise to improved charge transfer kinetics and eventually led to an increase in capacity over cycling. This intriguing observation has important implications for the development of titanium niobium oxides, which are potential anode material candidates that could be used as alternatives to graphite. The oxides of Ti and Nb are metastable phases because they can maintain their structural integrity due to kinetic hindrance toward their decomposition.[43] Moreover, some oxides, e.g., $TiNb_2O_7$, suffer from amorphization during their cycling, which leads to capacity fading.[42] Unlike other titanium niobium oxide analogues, however, our results revealed that the capacity of nanostructured TNO can increase upon amorphization. Therefore, we envision that this novel electrochemical behavior may provide an interesting new direction to tune titanium niobium oxides for high-performance, stable battery anodes.

■ ASSOCIATED CONTENT

Supporting Information

The Supporting Information is available free of charge at https://pubs.acs.org/doi/10.1021/acsami.3c05324.

Additional characterization and electrochemical analysis results (PDF)

■ AUTHOR INFORMATION

Corresponding Authors

Muhammad A. Abbas − *Nanosensor Research Institute, Hanyang University, Ansan, Gyeonggi-do 15588, Republic of Korea;* orcid.org/0000-0002-8338-9802; Email: mawaisabass@hanyang.ac.kr

Jin Ho Bang − *Nanosensor Research Institute and Department of Chemical and Molecular Engineering and Department of Applied Chemistry, Center for Bionano Intelligence Education and Research, Hanyang University, Ansan, Gyeonggi-do 15588, Republic of Korea;* orcid.org/0000-0002-6717-3454; Email: jbang@hanyang.ac.kr

Authors

Sang-eun Bak − *Department of Bionano Technology, Hanyang University, Ansan, Gyeonggi-do 15588, Republic of Korea*

Woowon Chung − *Department of Bionano Technology, Hanyang University, Ansan, Gyeonggi-do 15588, Republic of Korea*

Complete contact information is available at: https://pubs.acs.org/10.1021/acsami.3c05324

Notes

The authors declare no competing financial interest.

■ ACKNOWLEDGMENTS

This work was supported by a grant from the Basic Science Research Program through the National Research Foundation (NRF) of Korea funded by the Ministry of Science and ICT (NRF-2022R1A2C2006654 and NRF-2020R1C1C1008588) and by the Ministry of Education (NRF-2018R1A6A1A03024231).

■ REFERENCES

(1) Li, J.; Fleetwood, J.; Hawley, W. B.; Kays, W. From Materials to Cell: State-of-the-Art and Prospective Technologies for Lithium-Ion Battery Electrode Processing. *Chem. Rev.* **2022**, *122*, 903−956.

(2) Lei, T.; Gu, M.; Fu, H.; Wang, J.; Wang, L.; Zhou, J.; Liu, H.; Lu, B. Bond Modulation of $MoSe_{2+x}$ Driving Combined Intercalation and Conversion Reactions for High-Performance K Cathodes. *Chem. Sci.* **2023**, *14*, 2528−2536.

(3) Wu, L.; Fu, H.; Li, S.; Zhu, J.; Zhou, J.; Rao, A. M.; Cha, L.; Guo, K.; Wen, S.; Lu, B. Phase-Engineered Cathode for Super-Stable Potassium Storage. *Nat. Commun.* **2023**, *14*, 644.

(4) Tian, Y.; Zeng, G.; Rutt, A.; Shi, T.; Kim, H.; Wang, J.; Koettgen, J.; Sun, Y.; Ouyang, B.; Chen, T.; Lun, Z.; Rong, Z.; Persson, K.; Ceder, G. Promises and Challenges of Next-Generation "Beyond Li-Ion" Batteries for Electric Vehicles and Grid Decarbonization. *Chem. Rev.* **2021**, *121*, 1623−1669.

(5) Manthiram, A. An Outlook on Lithium Ion Battery Technology. *ACS Cent. Sci.* **2017**, *3*, 1063−1069.

(6) Lee, M. D.; Lee, G. J.; Nam, I.; Abbas, M. A.; Bang, J. H. Exploring the Effect of Cation Vacancies in TiO_2: Lithiation Behavior of n-Type and p-Type TiO_2. *ACS Appl. Mater. Interfaces* **2022**, *14*, 6560−6569.

(7) Ye, H.; Zhang, Y.; Yin, Y.-X.; Cao, F.-F.; Guo, Y.-G. An Outlook on Low-Volume-Change Lithium Metal Anodes for Long-Life Batteries. *ACS Cent. Sci.* **2020**, *6*, 661−671.

(8) Wang, Y.; Liu, J.; Chen, T.; Lin, W.; Zheng, J. Factors That Affect Volume Change During Electrochemical Cycling in Cathode Materials for Lithium Ion Batteries. *Phys. Chem. Chem. Phys.* **2022**, *24*, 2167−2175.

(9) Choi, W. H.; Lee, C. H.; Kim, H.-e.; Lee, S. U.; Bang, J. H. Designing a High-Performance Nitrogen-Doped Titanium Dioxide

Anode Material for Lithium-Ion Batteries by Unravelling the Nitrogen Doping Effect. *Nano Energy* **2020**, *74*, 104829.
(10) Kim, H.-e.; Jang, S.; Lim, H.; Chung, W.; Nam, I.; Bang, J. H. Noble Metal Single-Atoms for Lithium-Ion Batteries: A Booster for Ultrafast Charging/Discharging in Carbon Electrodes. *Appl. Surf. Sci.* **2023**, *624*, 157161.
(11) Gu, M.; Rao, A. M.; Zhou, J.; Lu, B. In Situ Formed Uniform and Elastic SEI for High-Performance Batteries. *Energy Environ. Sci.* **2023**, *16*, 1166−1175.
(12) Choi, Y. S.; Choi, W.; Yoon, W.-S.; Kim, J. M. Unveiling the Genesis and Effectiveness of Negative Fading in Nanostructured Iron Oxide Anode Materials for Lithium-Ion Batteries. *ACS Nano* **2022**, *16*, 631−642.
(13) Kim, H.; Choi, W.; Yoon, J.; Um, J. H.; Lee, W.; Kim, J.; Cabana, J.; Yoon, W.-S. Exploring Anomalous Charge Storage in Anode Materials for Next-Generation Li Rechargeable Batteries. *Chem. Rev.* **2020**, *120*, 6934−6976.
(14) Edström, K.; Herstedt, M.; Abraham, D. P. A New Look at the Solid Electrolyte Interphase on Graphite Anodes in Li-Ion Batteries. *J. Power Sources* **2006**, *153*, 380−384.
(15) Goodenough, J. B.; Park, K.-S. The Li-Ion Rechargeable Battery: A Perspective. *J. Am. Chem. Soc.* **2013**, *135*, 1167−1176.
(16) Cheng, H.; Sun, Q.; Li, L.; Zou, Y.; Wang, Y.; Cai, T.; Zhao, F.; Liu, G.; Ma, Z.; Wahyudi, W.; Li, Q.; Ming, J. Emerging Era of Electrolyte Solvation Structure and Interfacial Model in Batteries. *ACS Energy Lett.* **2022**, *7*, 490−513.
(17) Adenusi, H.; Chass, G. A.; Passerini, S.; Tian, K. V.; Chen, G. Lithium Batteries and the Solid Electrolyte Interphase (SEI)—Progress and Outlook. *Adv. Energy Mater.* **2023**, *13*, 2203307.
(18) Poizot, P.; Laruelle, S.; Grugeon, S.; Dupont, L.; Tarascon, J. M. From the Vanadates to 3d-Metal Oxides Negative Electrodes. *Ionics* **2000**, *6*, 321−330.
(19) Grugeon, S.; Laruelle, S.; Herrera-Urbina, R.; Dupont, L.; Poizot, P.; Tarascon, J. M. Particle Size Effects on the Electrochemical Performance of Copper Oxides toward Lithium. *J. Electrochem. Soc.* **2001**, *148*, A285.
(20) Rezvani, S. J.; Gunnella, R.; Witkowska, A.; Mueller, F.; Pasqualini, M.; Nobili, F.; Passerini, S.; Cicco, A. D. Is the Solid Electrolyte Interphase an Extra-Charge Reservoir in Li-Ion Batteries? *ACS Appl. Mater. Interfaces* **2017**, *9*, 4570−4576.
(21) Jamnik, J.; Maier, J. Nanocrystallinity Effects in Lithium Battery Materials Aspects of Nano-Ionics. Part IV. *Phys. Chem. Chem. Phys.* **2003**, *5*, 5215−5220.
(22) Li, H.; Richter, G.; Maier, J. Reversible Formation and Decomposition of LiF Clusters Using Transition Metal Fluorides as Precursors and Their Application in Rechargeable Li Batteries. *Adv. Mater.* **2003**, *15*, 736−739.
(23) Zhukovskii, Y. F.; Balaya, P.; Kotomin, E. A.; Maier, J. Evidence for Interfacial-Storage Anomaly in Nanocomposites for Lithium Batteries from First-Principles Simulations. *Phys. Rev. Lett.* **2006**, *96*, 058302.
(24) Zhukovskii, Y. F.; Balaya, P.; Dolle, M.; Kotomin, E. A.; Maier, J. Enhanced Lithium Storage and Chemical Diffusion in Metal-LiF Nanocomposites: Experimental and Theoretical Results. *Phys. Rev. B: Condens. Matter Mater. Phys.* **2007**, *76*, 235414.
(25) Poizot, P.; Laruelle, S.; Grugeon, S.; Dupont, L.; Tarascon, J. M. Nano-Sized Transition-Metal Oxides as Negative-Electrode Materials for Lithium-Ion Batteries. *Nature* **2000**, *407*, 496−499.
(26) Hu, Y.-Y.; Liu, Z.; Nam, K.-W.; Borkiewicz, O. J.; Cheng, J.; Hua, X.; Dunstan, M. T.; Yu, X.; Wiaderek, K. M.; Du, L.-S.; Chapman, K. W.; Chupas, P. J.; Yang, X.-Q.; Grey, C. P. Origin of Additional Capacities in Metal Oxide Lithium-Ion Battery Electrodes. *Nat. Mater.* **2013**, *12*, 1130−1136.
(27) Griffith, K. J.; Harada, Y.; Egusa, S.; Ribas, R. M.; Monteiro, R. S.; Von Dreele, R. B.; Cheetham, A. K.; Cava, R. J.; Grey, C. P.; Goodenough, J. B. Titanium Niobium Oxide: From Discovery to Application in Fast-Charging Lithium-Ion Batteries. *Chem. Mater.* **2021**, *33*, 4−18.
(28) Bak, S.-e.; Chung, W.; Abbas, M. A.; Bang, J. H. Evidence of Intrinsic Pseudocapacitive Lithium Intercalation in Rutile $TiNbO_4$. *ACS Appl. Energy Mater.* **2022**, *5*, 5508−5512.
(29) Lee, J.; Kwak, H. H.; Bak, S.-e.; Lee, G. J.; Hong, S.-T.; Abbas, M. A.; Bang, J. H. New Class of Titanium Niobium Oxide for a Li-Ion Host: $TiNbO_4$ with Purely Single-Phase Lithium Intercalation. *Chem. Mater.* **2022**, *34*, 854−863.
(30) Gogotsi, Y.; Penner, R. M. Energy Storage in Nanomaterials − Capacitive, Pseudocapacitive, or Battery-Like? *ACS Nano* **2018**, *12*, 2081−2083.
(31) Augustyn, V.; Simon, P.; Dunn, B. Pseudocapacitive Oxide Materials for High-Rate Electrochemical Energy Storage. *Energy Environ. Sci.* **2014**, *7*, 1597−1614.
(32) Park, K.-J.; Lim, B.-B.; Choi, M.-H.; Jung, H.-G.; Sun, Y.-K.; Haro, M.; Vicente, N.; Bisquert, J.; Garcia-Belmonte, G. A High-Capacity $Li[Ni_{0.8}Co_{0.06}Mn_{0.14}]O_2$ Positive Electrode with a Dual Concentration Gradient for Next-Generation Lithium-Ion Batteries. *J. Mater. Chem. A* **2015**, *3*, 22183−22190.
(33) Haro, M.; Song, T.; Guerrero, A.; Bertoluzzi, L.; Bisquert, J.; Paik, U.; Garcia-Belmonte, G. Germanium Coating Boosts Lithium Uptake in Si Nanotube Battery Anodes. *Phys. Chem. Chem. Phys.* **2014**, *16*, 17930−17935.
(34) Lim, H.; Abbas, M. A.; Bang, J. H. Memory Effect in Lithium Titanate Driven by Interfacial Oxygen Vacancies. *ACS Energy Lett.* **2022**, *7*, 1086−1091.
(35) Lee, G. J.; Abbas, M. A.; Lee, M. D.; Lee, J.; Lee, J.; Bang, J. H. Lithiation Mechanism Change Driven by Thermally Induced Grain Fining and Its Impact on the Performance of $LiMn_2O_4$ in Lithium-Ion Batteries. *Small* **2020**, *16*, 2002292.
(36) Shim, J.; Bang, J. H. Overlooked Impact of Precursor Mixing: Implications in the Electrochemical Performance of Battery Electrode Materials. *J. Energy Chem.* **2023**, *82*, 56−65.
(37) Sun, H.; Xin, G.; Hu, T.; Yu, M.; Shao, D.; Sun, X.; Lian, J. High-Rate Lithiation-Induced Reactivation of Mesoporous Hollow Spheres for Long-Lived Lithium-Ion Batteries. *Nat. Commun.* **2014**, *5*, 4526.
(38) Martin, L.; Martinez, H.; Poinot, D.; Pecquenard, B.; Le Cras, F. Direct Observation of Important Morphology and Composition Changes at the Surface of the CuO Conversion Material in Lithium Batteries. *J. Power Sources* **2014**, *248*, 861−873.
(39) Balaya, P.; Li, H.; Kienle, L.; Maier, J. Fully Reversible Homogeneous and Heterogeneous Li Storage in RuO_2 with High Capacity. *Adv. Funct. Mater.* **2003**, *13*, 621−625.
(40) Aragón, M. J.; León, B.; Pérez Vicente, C.; Tirado, J. L. A New Form of Manganese Carbonate for the Negative Electrode of Lithium-Ion Batteries. *J. Power Sources* **2011**, *196*, 2863−2866.
(41) Aragón, M. J.; León, B.; Pérez Vicente, C.; Tirado, J. L. On the Use of Transition Metal Oxysalts as Conversion Electrodes in Lithium-Ion Batteries. *J. Power Sources* **2009**, *189*, 823−827.
(42) Chung, W.; Bang, J. H. Carbon-Doped $TiNb_2O_7$ Suppresses Amorphization-Induced Capacity Fading. *ACS Appl. Mater. Interfaces* **2022**, *14*, 19365−19375.
(43) Voskanyan, A. A.; Abramchuk, M.; Navrotsky, A. Entropy Stabilization of TiO_2−Nb_2O_5 Wadsley−Roth Shear Phases and Their Prospects for Lithium-Ion Battery Anode Materials. *Chem. Mater.* **2020**, *32*, 5301−5308.

https://doi.org/10.1021/acsami.3c05324
ACS Appl. Mater. Interfaces 2023, 15, 34874−34882